

Recent increase in oceanic carbon uptake driven by weaker upper-ocean overturning

Tim DeVries^{1,2}, Mark Holzer^{3,4} & Francois Primeau⁵

The ocean is the largest sink for anthropogenic carbon dioxide (CO₂), having absorbed roughly 40 per cent of CO₂ emissions since the beginning of the industrial era^{1,2}. Recent data show that oceanic CO₂ uptake rates have been growing over the past decade^{3–7}, reversing a trend of stagnant or declining carbon uptake during the 1990s^{8–14}. Here we show that ocean circulation variability is the primary driver of these changes in oceanic CO₂ uptake over the past several decades. We use a global inverse model to quantify the mean ocean circulation during the 1980s, 1990s and 2000s, and then estimate the impact of decadal circulation changes on the oceanic CO₂ sink using a carbon cycling model. We find that during the 1990s an enhanced upper-ocean overturning circulation drove increased outgassing of natural CO₂, thus weakening the global CO₂ sink. This trend reversed during the 2000s as the overturning circulation weakened. Continued weakening of the upper-ocean overturning is likely to strengthen the CO₂ sink in the near future by trapping natural CO₂ in the deep ocean, but ultimately may limit oceanic uptake of anthropogenic CO₂.

Surface CO₂ observations have revealed large decadal variability in the oceanic CO₂ sink, with a substantial increase in ocean carbon uptake over the last decade^{7,15}. However, attributing this variability to specific mechanisms remains a challenge. This is because multiple factors influence ocean CO₂ uptake rates, including sea surface temperature (SST) and chemistry, biological CO₂ utilization, and ocean circulation patterns. Measured sea surface CO₂ concentrations integrate all these factors, making it difficult to disentangle the influence of each on the changing oceanic CO₂ sink.

Here we diagnose the effects of ocean circulation variability on the oceanic CO₂ sink over the past several decades. We assimilate oceanographic tracer observations into an ocean circulation inverse model^{2,16} to estimate the decadal-mean circulation of the 1980s, 1990s and 2000s (see Methods). We focus on depths shallower than 1,000 m (defining the ‘upper ocean’) because deeper waters are not likely to exchange with the atmosphere on the decadal timescales considered. The diagnosed circulation in all three time periods is characterized by upwelling in the Antarctic, equatorial, and northern subpolar regions (Fig. 1). This upwelling is balanced by subtropical downwelling in both hemispheres, driven by the convergence of wind-driven surface currents. The subduction of water masses in the subtropics provides a pathway for the transport of anthropogenic CO₂ to greater depths¹⁷, although much of the carbon transported along this pathway is rapidly upwelled in the tropics¹⁸. We refer to these patterns of upwelling and downwelling in the upper ocean, which transport and exchange carbon within the upper 1,000 m, as the ‘upper-ocean overturning circulation’. This circulation consists of the shallow components of the major deep-ocean overturning cells of the North Atlantic and Southern Ocean, as well as shallower overturning cells associated with the formation and destruction of intermediate and mode waters in the sub-polar and sub-tropical regions.

The diagnosed upper-ocean overturning circulation rates vary by up to 50% from one decade to the next. The upper-ocean overturning increased in the 1990s relative to the 1980s, particularly in the Southern Hemisphere (Fig. 1b). This is consistent with the expected response to intensified Southern Hemisphere westerly winds associated with a positive phase of the Southern Annular Mode (or Antarctic Oscillation) during this time period^{10,19}. This enhanced wind-driven circulation led to a roughly 40% increase in upwelling in the Antarctic region, consistent with enhanced Ekman suction⁷. The subduction of Southern Hemisphere subtropical waters increased by about 20% over the previous decade, and tropical upwelling across 200 m increased from 21 Sv to 31 Sv (Fig. 1b). In the Northern Hemisphere, volume flow rates in the 1990s were broadly similar to those in the 1980s. Natural variability in the North Atlantic meridional overturning circulation appears to be closely linked with the North Atlantic Oscillation, which was positive during the early 1990s and negative during the latter half of the decade²⁰. Our effective decadal circulations probably average over much of this interannual variability. Nonetheless, for the 1990s the assimilation estimates slightly enhanced northward surface transports into the subtropical gyre, which increased the formation rate of subtropical North Atlantic mode waters (Extended Data Fig. 1).

Our data assimilation model estimates a weaker upper-ocean overturning circulation in the 2000s compared to the 1990s (Fig. 1c). Southern Ocean upwelling associated with Ekman divergence south of the polar front decreased, and Ekman transport in the surface layer and downwelling in the southern subtropical gyres was also reduced. This was accompanied by a decline in subtropical downwelling and subpolar upwelling in the Northern Hemisphere (Fig. 1c). In the Atlantic, northward transport in the upper 1,000 m by the Atlantic Meridional Overturning Circulation showed a decrease of 1 ± 1 Sv (Extended Data Fig. 1), which is consistent with satellite altimetry and cable measurements that show large interannual variability in the Atlantic Meridional Overturning Circulation but little detectable trend over the last two decades²¹. This indicates that the inferred circulation changes are not necessarily connected with variability in the deep overturning cells (Extended Data Fig. 2). Our model also diagnoses a decrease in tropical upwelling during the 2000s, which might seem at odds with the strengthened trade winds for this period. However, model simulations show that enhanced trade winds drive anomalous upwelling that is localized near the Equator and above approximately 100 m in the central and eastern Pacific²². Consistent with this expectation, our diagnosed shallow equatorial Pacific upwelling (through 100 m, between 8° S and 8° N) increased from 27 Sv during the 1990s to 32 Sv during the 2000s.

How have these circulation changes affected the oceanic CO₂ sink? To examine this, we coupled an ocean carbon cycle model to the data-assimilated ocean circulation model, and simulated the transient evolution of dissolved inorganic carbon (DIC) from 1765 to 2014 (see Methods). These simulations reveal that changes in ocean circulation

¹Department of Geography, University of California, Santa Barbara, California 93106, USA. ²Earth Research Institute, University of California, Santa Barbara, California 93106, USA. ³School of Mathematics and Statistics, University of New South Wales, Sydney, New South Wales 2052, Australia. ⁴Department of Applied Physics and Applied Mathematics, Columbia University, New York, New York 10027, USA. ⁵Department of Earth System Science, University of California, Irvine, California 92697, USA.

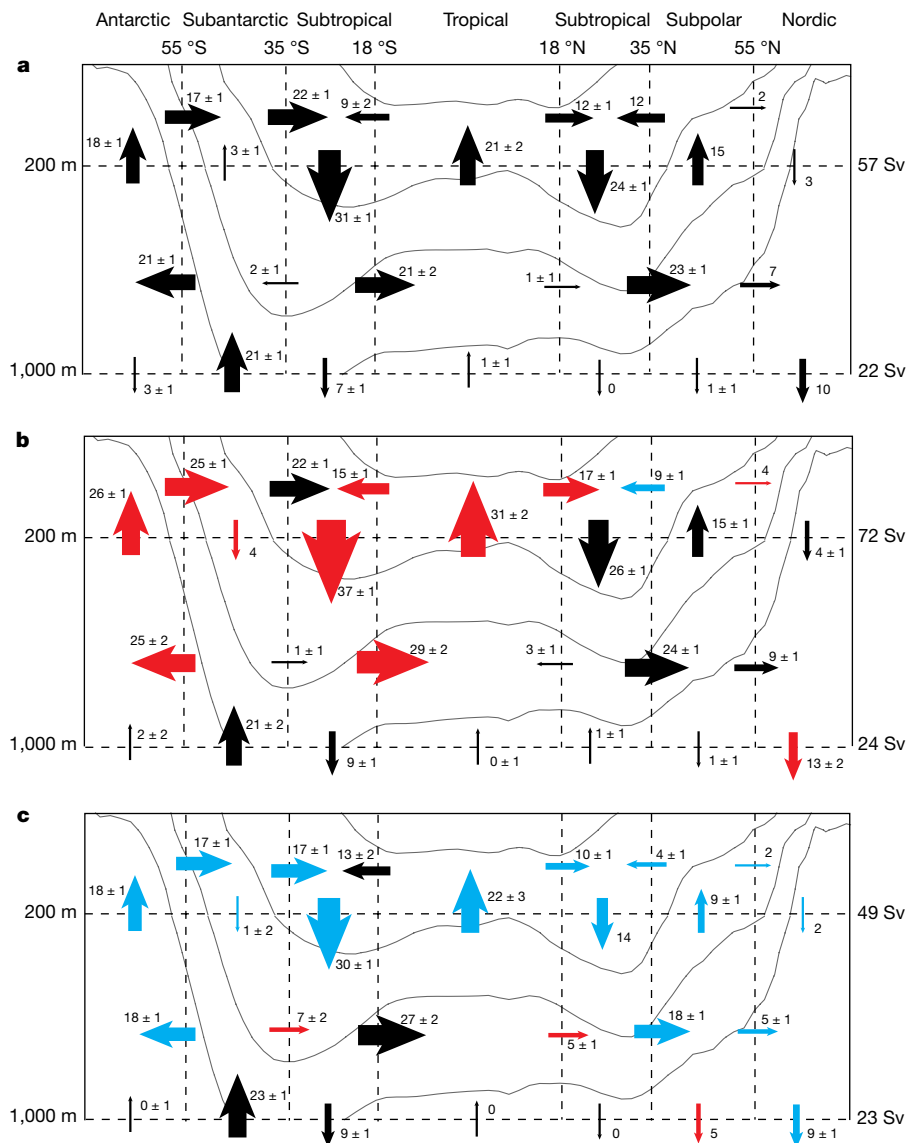


Figure 1 | Upper-ocean overturning circulation during the last three decades. Volume transports are shown in units of Sverdrup (Sv; $10^6 \text{ m}^3 \text{ s}^{-1}$) for the 1980s (1980–1989) (a), 1990s (1990–1999) (b) and 2000s (2000–2010) (c). Red (blue) arrows indicate an increase (decrease) in the magnitude of the transport relative to the previous decade. Thin grey lines indicate the mean position of isopycnals with density $\sigma_\theta = 25.4 \text{ kg m}^{-3}$, 26.6 kg m^{-3} , 27.2 kg m^{-3} and 27.6 kg m^{-3} . Uncertainties are standard deviations calculated from a suite of five different data-assimilated circulation models (Supplementary Table 1). To the right of each diagram is the total exchange of waters across each depth horizon. The 200-m depth roughly corresponds to the base of the surface mixed layer, while the 1,000-m depth corresponds to the base of the mesopelagic layer.

over the past two decades have driven substantial variability in ocean CO_2 uptake (Fig. 2). Oceanic CO_2 uptake decreased during the 1990s owing to the strengthened upper-ocean overturning during this period. Despite an increase in atmospheric CO_2 , net oceanic CO_2 uptake dropped from about 1.7 Pg C yr^{-1} in the 1980s to about 1.3 Pg C yr^{-1} in the 1990s (Fig. 2a). The largest reduction in oceanic CO_2 storage rates occurred in the sub-Antarctic, where storage rates dropped to $0.12 \text{ Pg C yr}^{-1}$, which is 0.3 Pg C yr^{-1} lower than they would have been had the circulation remained constant (Fig. 2a). This finding is consistent with a weakening of the Southern Ocean CO_2 sink during the 1990s that has been predicted by prognostic ocean models^{8,19} and detected in inversions of atmospheric and oceanic CO_2 data^{3,10}.

The weaker upper-ocean overturning circulation during the 2000s led to an increase in the global ocean CO_2 sink (Fig. 2b). Southern Ocean CO_2 uptake has increased by more than 50%, primarily owing to reduced outgassing of natural CO_2 (Extended Data Fig. 3) in response to reduced upwelling associated with weaker northward surface flows (Fig. 1). Consistent with analyses of surface-ocean records of the partial pressure of CO_2 , p_{CO_2} (ref. 7), we find that the Atlantic and Indian sectors account for most of the increase in Southern Ocean CO_2 uptake, while circulation variability has a more ambiguous effect on CO_2 uptake in the Pacific sector of the Southern Ocean (Fig. 2b). Outgassing of CO_2 in the tropics during the 2000s decreased to about 50% of its 1990s value, with reduced upwelling accounting for a large

increase in CO_2 uptake in the tropics (Fig. 2b). As in the Southern Ocean, the enhanced tropical CO_2 sink is driven primarily by the Atlantic and Indian Ocean, in agreement with uptake rates diagnosed from surface p_{CO_2} observations²³. CO_2 fluxes in the equatorial Pacific have been shown to exhibit strong interannual variability owing to the influence of the El Niño/Southern Oscillation²³, which is averaged out by our decadal-mean model. Finally, a reduction in shallow overturning circulation (Extended Data Fig. 2) also drove increased CO_2 uptake in the subtropical North Atlantic, the subtropical South Pacific, and the subpolar North Pacific (Fig. 2b).

The diagnosed decadal variability of the oceanic CO_2 sink is directly linked to variations in the strength of the upper-ocean overturning circulation (Fig. 3). Vigorous overturning, as in the 1990s, brings DIC-enriched deep waters to the surface, where the carbon outgasses to the atmosphere. (The resulting increase in surface DIC is partially countered by an increase in surface alkalinity, an effect taken into account by our model.) These deep waters are enriched in DIC by the action of the biological carbon pump, an effect independent of rising atmospheric CO_2 concentrations and therefore considered part of the ‘natural’ oceanic DIC distribution. At the same time, a vigorous upper-ocean overturning circulation promotes the formation of intermediate and mode waters that bring anthropogenic CO_2 into the deeper ocean, enhancing the ocean’s ability to absorb anthropogenic CO_2 . Weaker upper-ocean overturning, as in the 2000s, has the

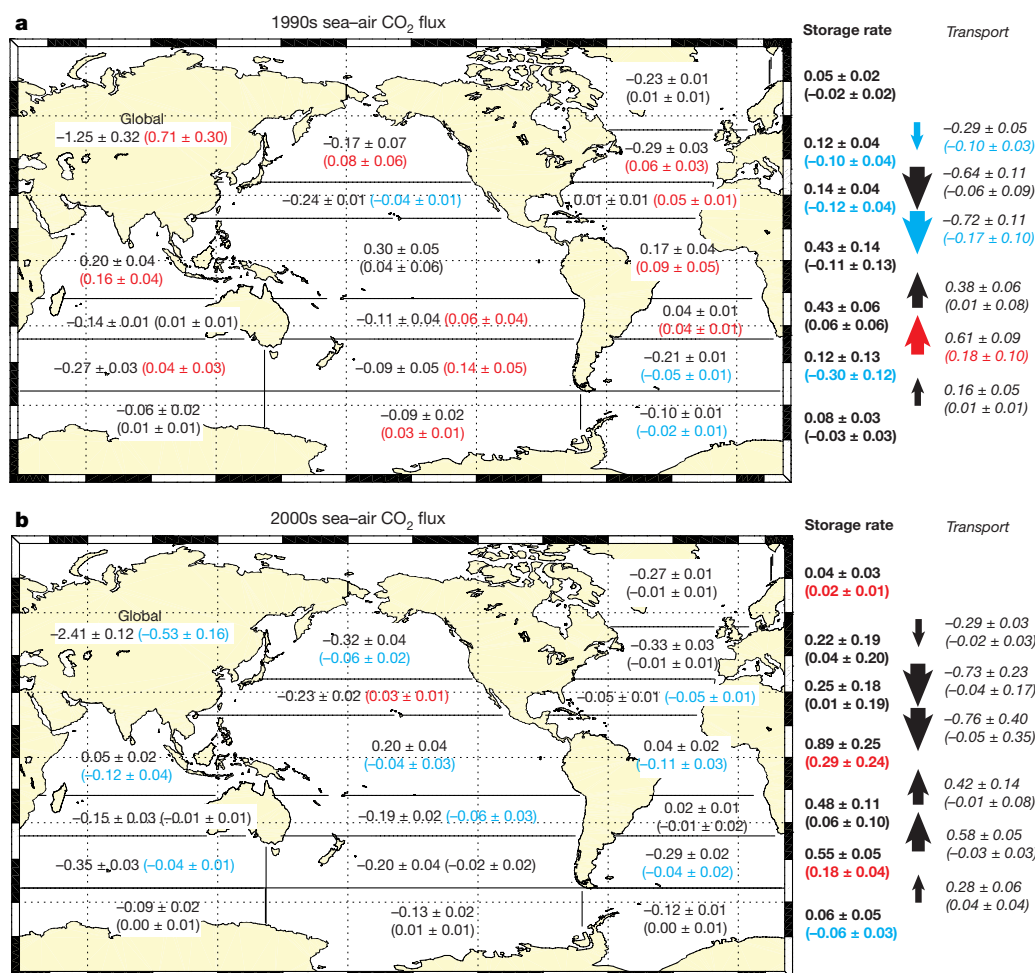


Figure 2 | Global and regional decadal variability of the oceanic CO₂ sink. The decadal averaged air–sea CO₂ flux, carbon storage rate (in boldface), and rate of carbon transport (in italics), for the 1990s (a) and the 2000s (b). Units are Pg C yr⁻¹. Geographic regions are as in Fig. 1, with air–sea fluxes (negative values indicate ocean uptake) further partitioned by ocean basin. Storage rates and transports (positive values indicate northward) are integrated zonally over the entire water column. Numbers in parentheses indicate the anomalous CO₂ flux, storage, or northward

transport driven by circulation variability (see Methods), with colours indicating that circulation variability drove a significant (that is, the mean is greater than the uncertainty) increase (red) or decrease (blue) in each quantity relative to the previous decade. Uncertainties are standard deviations calculated from a suite of 160 model simulations which varied parameters of the physical and biogeochemical models (Supplementary Tables 1 and 2).

opposite effect, suppressing the outgassing of natural CO₂ and the uptake of anthropogenic CO₂. The net effect of these two competing mechanisms in the 1990s was to enhance the outgassing of natural CO₂ by about 0.9 Pg of carbon per year (Pg C yr⁻¹), while enhancing the uptake of anthropogenic CO₂ by about 0.2 Pg C yr⁻¹ (Fig. 3a, b). Weaker overturning in the 2000s has enhanced the oceanic sink of natural CO₂ by about 0.6 Pg C yr⁻¹, and reduced the oceanic uptake of anthropogenic CO₂ by about 0.1 Pg C yr⁻¹ (Fig. 3c, d; Extended Data Figs 3 and 4).

These calculations (Figs 2 and 3) isolate the effect of circulation variability on the oceanic CO₂ sink, but do not take into account thermal (solubility) and biological effects. Thermal effects can be estimated by calculating the effects of observed SST variations on air–sea CO₂ fluxes. In simulations with decadal varying SST (see Methods), we find that thermal effects are roughly an order of magnitude less important than circulation variability for driving the decadal variability of oceanic CO₂ uptake (Extended Data Fig. 5). In some regions, the two effects are of similar magnitude, such as the Antarctic, where circulation changes have reduced CO₂ uptake while surface cooling has increased CO₂ uptake, in agreement with analyses of surface-ocean p_{CO_2} data⁵. However, in most other regions, circulation variability dominates thermal effects (Extended Data Fig. 5).

Our results are consistent with the emerging picture that oceanic CO₂ uptake has strengthened in recent years^{5,7,15,24}. Comparing our results with p_{CO_2} -based reconstructions of the ocean CO₂ sink from the Surface Ocean p_{CO_2} Mapping (SOCOM) project¹⁵ shows good agreement between these independent estimates, with a much stronger CO₂ sink in the 2000s compared to the 1990s (Extended Data Fig. 6). Perhaps the best metric for comparison is the trend in CO₂ uptake over the past decade. For the subset of SOCOM models exhibiting the best match to observed interannual variability, the trend in oceanic CO₂ uptake over the period 2001–2011 is about 0.8 Pg C yr⁻¹ per decade (ref. 15). Over the same period, the trend due to atmospheric CO₂ increase is ~0.4 Pg C yr⁻¹ per decade (ref. 2). Our results show that the additional 0.4 Pg C yr⁻¹ per decade of uptake can be explained by weakened overturning circulation (contributing about 0.5 ± 0.2 Pg C yr⁻¹ per decade of additional uptake; Fig. 2) combined with surface warming (contributing -0.08 ± 0.02 Pg C yr⁻¹ per decade; Extended Data Fig. 5). This suggests that biological effects might not contribute much to the recent intensification of the oceanic CO₂ sink.

What are the implications of these findings for the contemporary and future oceanic CO₂ sink? Models predict strengthening of the oceanic CO₂ sink in key regions such as the Southern Ocean²⁵ and the tropical Pacific²⁶ in response to weaker overturning circulation in the future.

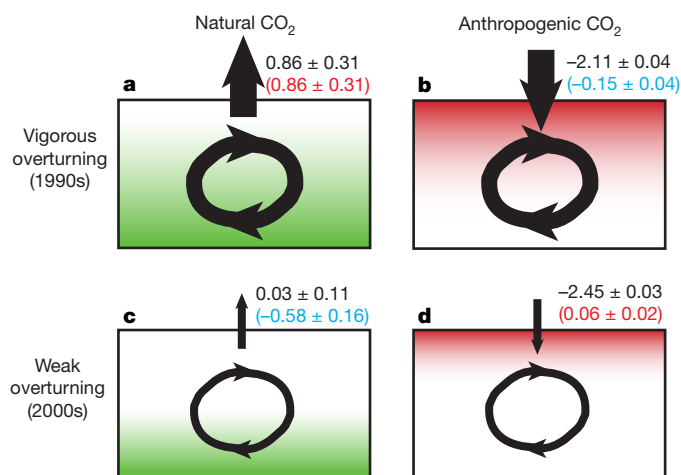


Figure 3 | Simplified conceptual diagram illustrating how changes in upper-ocean overturning circulation have affected the oceanic CO₂ sink. Vigorous overturning in the 1990s drove increased outgassing of natural CO₂ (a), and increased uptake of anthropogenic CO₂ (b). In the 2000s, weaker overturning has had the opposite effect, reducing the outgassing of natural CO₂ (c) and the uptake of anthropogenic CO₂ (d). Black numbers indicate the globally integrated air–sea flux of each CO₂ component (Pg C yr⁻¹, negative values indicate ocean uptake), and include the increase in anthropogenic CO₂ uptake due to rising atmospheric CO₂. Numbers in parentheses represent the anomalous flux driven by circulation variability (see Methods). Colour scheme and uncertainties as in Fig. 2.

Our results suggest that this weakening trend may have already begun, at least in the upper ocean, driving the intensification of the oceanic CO₂ sink over the last decade. While the circulation changes diagnosed here are consistent with the expected response of the ocean circulation to anthropogenic forcing^{25,27}, our diagnostic model cannot separate the impact of natural variability from anthropogenic forcing. Given the strong natural variability in the oceanic CO₂ sink²⁸, it will be important to verify a reduction in overturning circulation over a multi-decadal period in order to attribute it definitively to anthropogenic forcing. If weakening continues in the future, this may help to enhance the oceanic CO₂ sink for some time. However, as anthropogenic CO₂ accumulates in the atmosphere, its reduced uptake by the ocean owing to weaker ventilation may eventually overwhelm the reduced efflux of natural CO₂, diminishing the ocean CO₂ sink²⁹. To track the timing and magnitude of these effects, the variability of the ocean circulation and CO₂ uptake must be monitored carefully over time.

Online Content Methods, along with any additional Extended Data display items and Source Data, are available in the online version of the paper; references unique to these sections appear only in the online paper.

Received 24 March; accepted 7 December 2016.

1. Khattiwala, S. *et al.* Global ocean storage of anthropogenic carbon. *Biogeosciences* **10**, 2169–2191 (2013).
2. DeVries, T. The oceanic anthropogenic CO₂ sink: storage, air–sea fluxes, and transports over the industrial era. *Glob. Biogeochem. Cycles* **28**, 631–647 (2014).
3. Fay, A. R. & McKinley, G. A. Global trends in surface ocean pCO₂ from in situ data. *Glob. Biogeochem. Cycles* **27**, 541–557 (2013).
4. Landschützer, P., Gruber, N., Bakker, D. C. E. & Schuster, U. Recent variability of the global ocean carbon sink. *Glob. Biogeochem. Cycles* **28**, 927–949 (2014).
5. Majkut, J. D., Sarmiento, J. & Rodgers, K. A growing oceanic carbon uptake: results from an inversion study of surface pCO₂ data. *Glob. Biogeochem. Cycles* **28**, 335–351 (2014).
6. Munro, D. R. *et al.* Recent evidence for a strengthening CO₂ sink in the Southern Ocean from carbonate system measurements in the Drake Passage (2002–2015). *Geophys. Res. Lett.* **42**, 7623–7630 (2015).

7. Landschützer, P. *et al.* The reinvigoration of the Southern Ocean carbon sink. *Science* **349**, 1221–1224 (2015).
8. Sarmiento, J. L. *et al.* Trends and regional distributions of land and ocean carbon sinks. *Biogeosciences* **7**, 2351–2367 (2010).
9. Schuster, U. & Watson, A. J. A variable and decreasing sink for atmospheric CO₂ in the North Atlantic. *J. Geophys. Res.* **112**, C11006 (2007).
10. Le Quére, C. *et al.* Saturation of the Southern Ocean CO₂ sink due to recent climate change. *Science* **316**, 1735–1738 (2007).
11. Le Quére, C. *et al.* Trends in the sources and sinks of carbon dioxide. *Nat. Geosci.* **2**, 831–836 (2009).
12. McKinley, G. A., Fay, A. R., Takahashi, T. & Metz, N. Convergence of atmospheric and North Atlantic carbon dioxide trends on multidecadal timescales. *Nat. Geosci.* **4**, 606–610 (2011).
13. Pérez, F. F. *et al.* Atlantic Ocean CO₂ uptake reduced by weakening of the meridional overturning circulation. *Nat. Geosci.* **6**, 146–152 (2013).
14. McNeil, B. & Matear, R. The non-steady state oceanic CO₂ signal: its importance, magnitude and a novel way to detect it. *Biogeosciences* **10**, 2219–2228 (2013).
15. Rödenbeck, C. *et al.* Data-based estimates of the ocean carbon sink variability: first results of the surface ocean pCO₂ mapping intercomparison (SOCOM). *Biogeosciences* **12**, 7251–7278 (2015).
16. DeVries, T. & Primeau, F. Dynamically and observationally constrained estimates of water-mass distributions and ages in the global ocean. *J. Phys. Oceanogr.* **41**, 2381–2401 (2011).
17. Bopp, L., Levy, M., Resplandy, L. & Saltee, J. B. Pathways of anthropogenic carbon subduction in the global ocean. *Geophys. Res. Lett.* **42**, 6416–6423 (2015).
18. Nakano, H., Ishii, M., Rodgers, K., Tsujino, H. & Yamanaka, G. Anthropogenic CO₂ uptake, transport, storage, and dynamical controls in the ocean imposed by the meridional overturning circulation: a modeling study. *Glob. Biogeochem. Cycles* **29**, 1706–1724 (2015).
19. Lovenduski, N. S., Gruber, N. & Doney, S. C. Toward a mechanistic understanding of the decadal trends in the Southern Ocean carbon sink. *Glob. Biogeochem. Cycles* **22**, GB3016 (2008).
20. Thomas, H. *et al.* Changes in the North Atlantic Oscillation influence CO₂ uptake in the North Atlantic over the past 2 decades. *Glob. Biogeochem. Cycles* **22**, GB4027 (2008).
21. Frajka-Williams, E. Estimating the Atlantic overturning at 26°N using satellite altimetry and cable measurements. *Geophys. Res. Lett.* **42**, 3458–3464 (2015).
22. England, M. H. *et al.* Recent intensification of wind-driven circulation in the Pacific and the ongoing warming hiatus. *Nat. Clim. Chang.* **4**, 222–227 (2014).
23. Landschützer, P., Gruber, N. & Bakker, D. C. E. Decadal variations and trends of the global ocean carbon sink. *Glob. Biogeochem. Cycles* **30**, 1396–1417 (2016).
24. Rödenbeck, C. *et al.* Interannual sea–air CO₂ flux variability from an observation-driven ocean mixed-layer scheme. *Biogeosciences* **11**, 4599–4613 (2014).
25. Ito, T. *et al.* Sustained growth of the Southern Ocean carbon storage in a warming climate. *Geophys. Res. Lett.* **42**, 4516–4522 (2015).
26. DiNezio, P. N., Barbero, L., Long, M. C., Lovenduski, N. & Deser, C. Are anthropogenic changes in the tropical ocean carbon cycle masked by Pacific Decadal Variability? *US CLIVAR Var.* **13**, 12–16, https://usclivar.org/sites/default/files/documents/2015/Variations2015Spring_0.pdf (2015).
27. Bernardello, R. *et al.* Response of the ocean natural carbon storage to projected twenty-first-century climate change. *J. Clim.* **27**, 2033–2053 (2014).
28. McKinley, G. A. *et al.* Timescales for detection of trends in the ocean carbon sink. *Nature* **530**, 469–472 (2016).
29. Bernardello, R., Marinov, I., Palter, J. B., Galbraith, E. D. & Sarmiento, J. L. Impact of Weddell Sea deep convection on natural and anthropogenic carbon in a climate model. *Geophys. Res. Lett.* **41**, 7262–7269 (2014).

Supplementary Information is available in the online version of the paper.

Acknowledgements T.D. acknowledges support from a University of California Regents Junior Faculty Fellowship, and from NASA grant NNX16A122G. M.H. acknowledges support from Australian Research Council grant DP120100674. F.P. acknowledges funding from the National Science Foundation award OCE 1436992. We thank all of the scientists who collected the oceanographic tracer data used in this study.

Author Contributions All authors conceived this study. T.D. performed the model simulations and analysed the data. T.D. wrote the manuscript with input from M.H. and F.P.

Author Information Reprints and permissions information is available at www.nature.com/reprints. The authors declare no competing financial interests. Readers are welcome to comment on the online version of the paper. Correspondence and requests for materials should be addressed to T.D. (tdevries@geog.ucsb.edu).

METHODS

Observational constraints for the data assimilation model. We used a data-assimilating ocean circulation inverse model (OCIM)^{2,16} to estimate the mean ocean circulation during three different time periods: pre-1990, the decade of the 1990s, and the period 2000–2014, which we refer to respectively as the 1980s, 1990s and 2000s. For each time period, we assimilated observations of five tracers: potential temperature, salinity, the chlorofluorocarbons CFC-11 and CFC-12, and $\Delta^{14}\text{C}$. Potential temperature and salinity data were taken from the 2013 World Ocean Database, Ocean Station Data and Profiling Floats data sets. The observations were binned by time period and then averaged onto the model grid. Quality control was performed by removing outliers (more than four inter-quartile ranges above the upper quartile) at each depth level in the model. This removed less than 0.1% of the observations. CFC-11, CFC-12 and $\Delta^{14}\text{C}$ observations were taken from the Global Ocean Data Analysis Project version 2 (GLODAPv2) database³⁰. These data were already quality-controlled. We used an earlier version of the GLODAPv2 database, but checking it against the newest release we find that the correlation R^2 of the fit between the CFC-11 and CFC-12 observations in each version is over 0.99. The only major difference between the version used and the newest version of GLODAPv2 is that the latter includes data from two additional cruise tracks in the Indian Ocean.

The CFC-11 and CFC-12 observations were binned by time period and then averaged onto the model grid. We assimilated $\Delta^{14}\text{C}$ observations only where they were paired with a near-zero CFC-11 or CFC-12 measurement (CFC-11 < 0.05 pmol kg⁻¹, CFC-12 < 0.025 pmol kg⁻¹). This was done to remove $\Delta^{14}\text{C}$ observations that may have been contaminated by bomb-produced ^{14}C , since we model only the ‘natural’ (pre-1955 bomb) component of $\Delta^{14}\text{C}$. These $\Delta^{14}\text{C}$ observations constrain the ventilation of deep water masses, and the same $\Delta^{14}\text{C}$ observations were used in each of the three assimilation periods.

Extended Data Fig. 7 shows the spatial distribution of the CFC observations for each decadal period, as well as the temporal distribution of observations of CFCs, temperature, and salinity. The spatial distributions of temperature and salinity are not shown, but all regions are well sampled for all time periods. Almost all of the transects with CFC observations in the 1990s were re-occupied with repeat hydrographies during the 2000s. During the 1980s, in contrast, several large areas are missing CFC observations. In particular, during the 1980s there are no CFC observations in the Pacific and Indian sectors of the Southern Ocean. For these sectors, the inferred circulation changes from the 1980s to the 1990s must therefore be interpreted cautiously. Nonetheless, the model-predicted weakening of the Southern Ocean CO_2 sink during the 1990s is in good agreement with independent studies using atmospheric inverse models¹⁰ and prognostic ocean general circulation models^{8,19}. This suggests that the more densely sampled temperature and salinity data, in conjunction with CFC data from elsewhere, may be able to compensate for a lack of CFC data in the Southern Ocean during the 1980s.

The sporadic nature of the oceanographic observations, particularly the CFC measurements (with some transects being occupied only about once per decade) makes the data assimilation susceptible to temporal aliasing. The error bars reported here do not take into account the uncertainty due to this potential aliasing of interannual variability into the data-assimilated circulations. Aliasing errors are likely to be largest for the smallest regions, and those with the sparsest observations. This must be kept in mind when interpreting the results of the assimilation model, particularly those on smaller spatial scales (for example, regional CO_2 fluxes of Fig. 2). On the other hand, these aliasing effects will be minimized when integrating over larger areas. Thus we would expect, for example, that the global CO_2 fluxes diagnosed by the assimilation model will be largely free from aliasing errors.

Finally, we note that in the Arctic Ocean and Mediterranean Sea, a combination of the small basin area and lack of data constraints causes the model CO_2 simulations to exhibit some numerical artefacts. We therefore do not include these regions in our analysis.

Tracer simulations and inversion procedure. We use an inversion procedure previously used to estimate the climatological mean state of the ocean circulation^{2,16}, and follow the methods used in those studies with a few exceptions, as detailed here. Here we break the assimilation down into three time periods: pre-1990, 1990–1999 and 2000–2014. We use the same dynamical forcing (wind stress and baroclinic pressure gradient forcing) for each time period. Then, tracer data from each period is assimilated independently to arrive at an estimate of the mean ocean circulation state during each period. This guarantees that the diagnosed circulation differences between time periods are due solely to information carried in the oceanographic tracer fields themselves, and not to assumptions about changes in external forcing. For each assimilation time period, we adjust a set of control parameters to minimize the misfit between observed and modelled tracer concentrations^{2,16}.

We note that this method yields a diagnostic, rather than predictive, estimate of ocean circulation within each assimilation time period. The approach therefore differs from that of standard coupled climate models such as those participating in Phase 5 of the Coupled Model Intercomparison Project (CMIP5). The CMIP5 models rely on the accuracy of external forcing and model physics to produce an accurate ocean state estimate. They therefore have relatively high spatial resolution (approximately 0.5° – 1°), resolve temporal variability on sub-daily timescales, and employ relatively sophisticated model physics. The OCIM, on the other hand, does not rely so much on the accuracy of external forcing or internal physics, but rather on the assimilation of global tracer data sets to produce an accurate ocean state estimate. To make this data assimilation tractable, the OCIM has relatively coarse resolution (2°), does not resolve temporal variability within assimilation time periods, and uses simplified linearized physics². The advantage of the OCIM relative to CMIP5 models is that the resulting circulation estimate is consistent with the observed tracer distributions, while the disadvantage is in its relatively coarse resolution and assumption of steady-state within each assimilation period.

In the OCIM, tracer concentrations C are simulated by solving the transport equation

$$\frac{dC}{dt} = AC + S(C) \quad (1)$$

where A is a matrix transport operator built from the model-estimated horizontal and vertical velocities and imposed diffusive terms, and $S(C)$ is a source–sink term. For the tracers simulated here the only sources and sinks are due to air–sea exchange, and except for the radioactive decay of ^{14}C they are conservative away from the surface layer. The source–sink term for these tracers takes the form

$$S(C) = \frac{K_w}{\delta z_1} (C_{\text{sat}} - C_{\text{surf}}) \quad (2)$$

which is non-zero only in the surface layer of the model (of thickness δz_1). The piston velocity K_w and the surface saturation concentration C_{sat} vary for each tracer. For potential temperature and salinity, $K_w = \delta z_1 / (30d)$, and C_{sat} is carried as a control (optimizable) parameter¹⁶, that is allowed to vary between assimilation time periods, but is held constant within each time period.

For CFC-11 and CFC-12, K_w is modelled as a quadratic function of wind speed 10 m above the sea surface, u (ref. 31)

$$K_w = a(1 - f_{\text{ice}})u^2(\text{Sc}/660)^{-1/2} \quad (3)$$

where a is a constant piston-velocity coefficient (consistent with a wind speed in metres per second and a piston velocity in centimetres per hour), f_{ice} is the fractional sea-ice cover, and Sc is the temperature-dependent Schmidt number. The 10-m wind speed and fractional sea-ice cover are taken from NCEP reanalysis for 1948–2014 and averaged for each year. For u the annual average is computed from daily values following the OCMIP-2 procedure³², which takes into account short-term variability in wind speeds. The surface saturation (C_{sat}) concentrations for CFC-11 and CFC-12 are computed from the observed time- and latitude-dependent atmospheric CFC-11 and CFC-12 concentrations³³ using a temperature- and salinity-dependent solubility³⁴. For the solubility we use time-independent temperatures and salinities from the 2009 World Ocean Atlas annual climatology^{35,36}. For CFC-11, our simulation runs from 1945 to 2014, and for CFC-12 from 1936 to 2014. Values for u and f_{ice} before 1948 are set to their 1948 values.

Natural radiocarbon is modelled in terms of the ratio $R = \Delta^{14}\text{C}/1,000 + 1$. The source–sink term of R takes the form

$$S(R) = \frac{1}{\tau_{\text{as}}} (1 - R_{\text{surf}}) - \frac{1}{\tau_d} R \quad (4)$$

The first term on the right-hand side represents the air–sea exchange with a well-mixed atmosphere of $R = 1$ (that is, $\Delta^{14}\text{C} = 0\text{‰}$) with a timescale $\tau_{\text{as}} = 5$ years, and is applied only in the top model layer. This simple parameterization neglects spatial variability in ^{14}C fluxes due to varying surface DIC and/or CO_2 fluxes, but is judged adequate for our purposes, because the $\Delta^{14}\text{C}$ constraint is needed only to constrain the approximate ventilation age distribution of the deep ocean, so that a reasonable distribution of respired DIC can be simulated. The second term on the right-hand side of equation (4) represents the radioactive decay of ^{14}C , with e-folding time $\tau_d = 8,266$ years, and is active throughout the water column. Biological sources and sinks of $\Delta^{14}\text{C}$ are neglected, because they have been shown to have a small effect on $\Delta^{14}\text{C}$ (ref. 37).

For most of the simulations here, we used a piston velocity coefficient of $a = 0.27$, following ref. 38. To test the sensitivity of our results to this value, we ran a set of assimilations with a increased by 30%, which is closer to the original OCMIP-2 value of $a = 0.337$ (ref. 32). In these assimilations we also reduced the

value of τ_{as} for the radiocarbon simulation by 30%, to be consistent with the higher assumed piston velocity. To get a sense of the uncertainty due to prescribed diffusivities, we also ran the model with different values of the isopycnal and vertical diffusivities, K_I and K_V . In all, we ran five different models with different values of a , K_I , and K_V . Supplementary Table 1 summarizes the fit to observations for each of these models for each assimilation period.

Extended Data Figs 8 and 9 show the zonally averaged difference between model-simulated and observed potential temperature (Extended Data Fig. 8) and CFC-11 (Extended Data Fig. 9) for the Atlantic and Pacific basins during each assimilation time period. The model-data residuals are small (generally less than 1 °C for potential temperature, and 0.5 pmol kg⁻¹ for CFC-11), but there are some biases. In the Atlantic, simulated potential temperatures are slightly too high in the northern subtropical thermocline, in the Southern Ocean upwelling region, and in the region of Antarctic Intermediate Water formation. Potential temperatures are slightly too low in the North Atlantic and in most of the thermocline. In the Pacific, these patterns are similar (Extended Data Fig. 8). Cooler-than-observed high latitudes are to be expected owing to the lack of seasonal cycle in the OCIM, which biases temperatures towards end-of-winter values. The most obvious bias in the CFC-11 field is a slight (about 0.25 pmol kg⁻¹) underprediction throughout most of the upper ocean. More negative biases (about 1 pmol kg⁻¹) occur in the surface of the Southern Ocean, the North Atlantic and the North Pacific (Extended Data Fig. 9). These negative biases could indicate that the CFC-11 piston velocity that we used for most simulations is too small. Because the same piston velocity was used for all assimilation periods, this would not affect the inferred circulation-driven changes in the CO₂ sink. Importantly, the spatial patterns of the model-data residuals are similar in all three assimilation time periods. This temporal coherence in the model-data residuals indicates that the inferred circulation changes do not introduce spurious biases into the assimilation.

Comparison with an unchanging ocean circulation. Our approach approximates the decadal variability of the ocean circulation by fitting a steady-state circulation independently for each time period. We thus neglect both interannual variability within, and temporal variations before, the assimilation period. However, the integrated effect of all previous circulation changes is encoded in the tracer distributions of the assimilation period, and therefore indirectly ascribed to an effective decadal circulation representative of the assimilation period.

To test whether these separate steady-state circulations for each time period capture the effects of the time-varying circulation, we used the data-assimilated circulations to simulate ocean CFC-11 concentrations, changing the circulation on the fly from decade to decade as the CFC-11 is propagated to the period of interest. We find that this approach fits the CFC-11 observations in each period much better than an unchanging circulation (Extended Data Fig. 10), which indicates that an unchanging circulation from decade-to-decade is not consistent with the tracer data. This also indicates that changing the circulation on the fly from decade to decade, as we did in our CO₂ simulations (see below), provides a good approximation to the effect of the continuously changing circulation of the ocean. **Ocean carbon-cycle model.** To investigate the influence of changing ocean circulation on the oceanic CO₂ sink we first simulated the pre-industrial carbon distribution (before 1765) by assuming that the ocean was in equilibrium with an atmospheric CO₂ concentration of 278 parts per million. We then simulated the transient evolution of dissolved inorganic carbon (DIC) from 1765 to 2014 using observed atmospheric CO₂ concentrations as a boundary condition². For this simulation, the ocean circulation is assumed to be steady-state before 1990 at its 1980s estimate, and is then switched abruptly to the assimilated circulations for the 1990s and 2000s. We acknowledge the approximate nature of this approach—the real ocean circulation changes gradually. We therefore present only decadal averaged results for the 1980s, 1990s and 2000s, rather than focusing on particular years. We estimated uncertainty by varying the parameters of the carbon-cycle model over a wide range of values. In all, we ran 32 simulations with different combinations of parameters governing the production and remineralization of particulate and dissolved organic carbon and calcium carbonate (Supplementary Table 2). Combined with five separate circulation estimates, we have 160 state estimates from which the uncertainties are derived.

For all simulations we used the OCMIP-2 formulation of the ocean carbon cycle³⁹, implemented for the matrix transport model as described elsewhere⁴⁰. The governing equation for the oceanic DIC concentration is

$$\frac{dDIC}{dt} = \mathbf{A} \times DIC + J_{v,DIC} + J_{g,DIC} + J_{b,DIC} \quad (5)$$

where \mathbf{A} is the matrix transport operator; $J_{v,DIC}$ is the virtual flux of DIC due to evaporation and precipitation; $J_{g,DIC}$ represents the air–sea gas exchange of CO₂; and $J_{b,DIC}$ are the biological transformations of DIC (uptake and remineralization of particulate and dissolved organic carbon). To compute the gas exchange fluxes of

CO₂ we must also simulate alkalinity—the equation for alkalinity follows equation (5) but without the air–sea exchange term. For our simulations, the only terms that vary from one time period to the next are \mathbf{A} (owing to variability in ocean circulation) and $J_{g,DIC}$ (owing to variability in the atmospheric CO₂ concentration and in the gas exchange piston velocity). The virtual fluxes and biological fluxes of DIC are held constant over time at their pre-industrial values, so that we can isolate the effects of ocean circulation variability on the oceanic CO₂ sink.

Air–sea CO₂ gas exchange occurs in the surface layer and is given by

$$J_{g,DIC} = \frac{K_w}{\delta z_1} ([CO_2]^{sat} - [CO_2]) \quad (6)$$

where the piston velocity is parameterized following equation (3). The CO₂ saturation concentrations are computed using observed temperature and salinity and the observed atmospheric p_{CO_2} . For the results presented in the main-text figures and in Extended Data Figs 3 and 4, we ignored changes in the solubility of CO₂ due to changes in SST and salinity, in order to isolate changes in ocean CO₂ uptake due to ocean circulation variability. For these simulations we calculated $[CO_2]^{sat}$ using the mean SST and salinity from the 2009 World Ocean Atlas objectively mapped climatologies^{35,36}. Atmospheric p_{CO_2} is taken from ref. 41 for the years 1765–2012, and from the Mauna Loa CO₂ record for the years 2013–2014.

The virtual fluxes $J_{v,DIC}$ and the biological carbon fluxes $J_{b,DIC}$ follow the OCMIP-2 design³⁹, and are implemented for the matrix transport model using a Newton solver as described elsewhere⁴⁰. Model parameters governing the biological cycling of carbon are listed in Supplementary Table 2. We allow for uncertainty in the parameters z_c (the compensation depth, above which DIC uptake is parameterized by restoring to observed PO₄ concentrations and multiplying by the globally constant ratio of C to P, $r_{C:P}$); the decay rate κ of labile dissolved organic phosphorus; the exponent b in the assumed power-law dependence of particle flux on depth⁴²; the CaCO₃:POC ‘rain ratio’ r ; and the e-folding depth d for CaCO₃ dissolution. These parameters are varied over a wide range to account for the range of values found in the literature^{32,39,40,43–50}, and are presented in Supplementary Table 2. Note that we do not vary σ , the fraction of production routed to dissolved organic phosphorus, because previous studies found that variations in κ and σ have very similar effects on DIC and alkalinity distributions⁴⁰. It is therefore sufficient to vary only κ . We also do not vary $r_{N:P}$ or $r_{C:P}$ as their values vary spatially in reality and are probably sensitive to the circulation which controls nutrient availability. These complexities are ignored here for expediency, and the biological cycling of DIC is assumed to be constant and unchanging, in order to isolate the direct effects of circulation changes.

To isolate the effects of circulation variability on the oceanic CO₂ sink (as in Figs 2 and 3), we ran two additional simulations which held the circulation at 1980s levels during the 1990s, and at 1990s levels during the 2000s. The anomalous CO₂ flux attributed to changing circulation during the 1990s was calculated as the difference between the 1990s CO₂ fluxes for the simulation in which the circulation was switched in 1990, and that in which the circulation remained at 1980s levels. Likewise, the anomalous CO₂ flux attributed to changing circulation during the 2000s was calculated as the difference between the 2000s CO₂ fluxes for the simulation in which the circulation was switched in 2000, and that in which the circulation remained at 1990s levels.

To diagnose the contribution of thermal effects on air–sea CO₂ fluxes, we also ran a suite of simulations in which we allowed $[CO_2]^{sat}$ to vary from one decade to the next owing to changes in SST. For these simulations, we calculated the decadal averaged SST for the 1980s, 1990s and 2000s from two different reconstructions, the Centennial *In situ* Observation-Based Estimates (COBE)⁵¹ and the Extended Reconstructed Sea Surface Temperature version 4 (ERSSTv4)⁵². For each decade, we calculated the anomaly with respect to the 1980s, and then added this anomaly to the climatological SST used in the model during the 1990s and 2000s. This yielded two separate reconstructed SST histories, which were used to compute the CO₂ saturation in separate simulations. Each simulation was run with each of the five different versions of our circulation model, yielding ten state estimates from which uncertainties were derived. The results of these simulations were then compared to otherwise identical simulations in which SSTs were held constant, and the difference between the two was attributed to thermal effects on CO₂ solubility. These differences are presented in Extended Data Fig. 5.

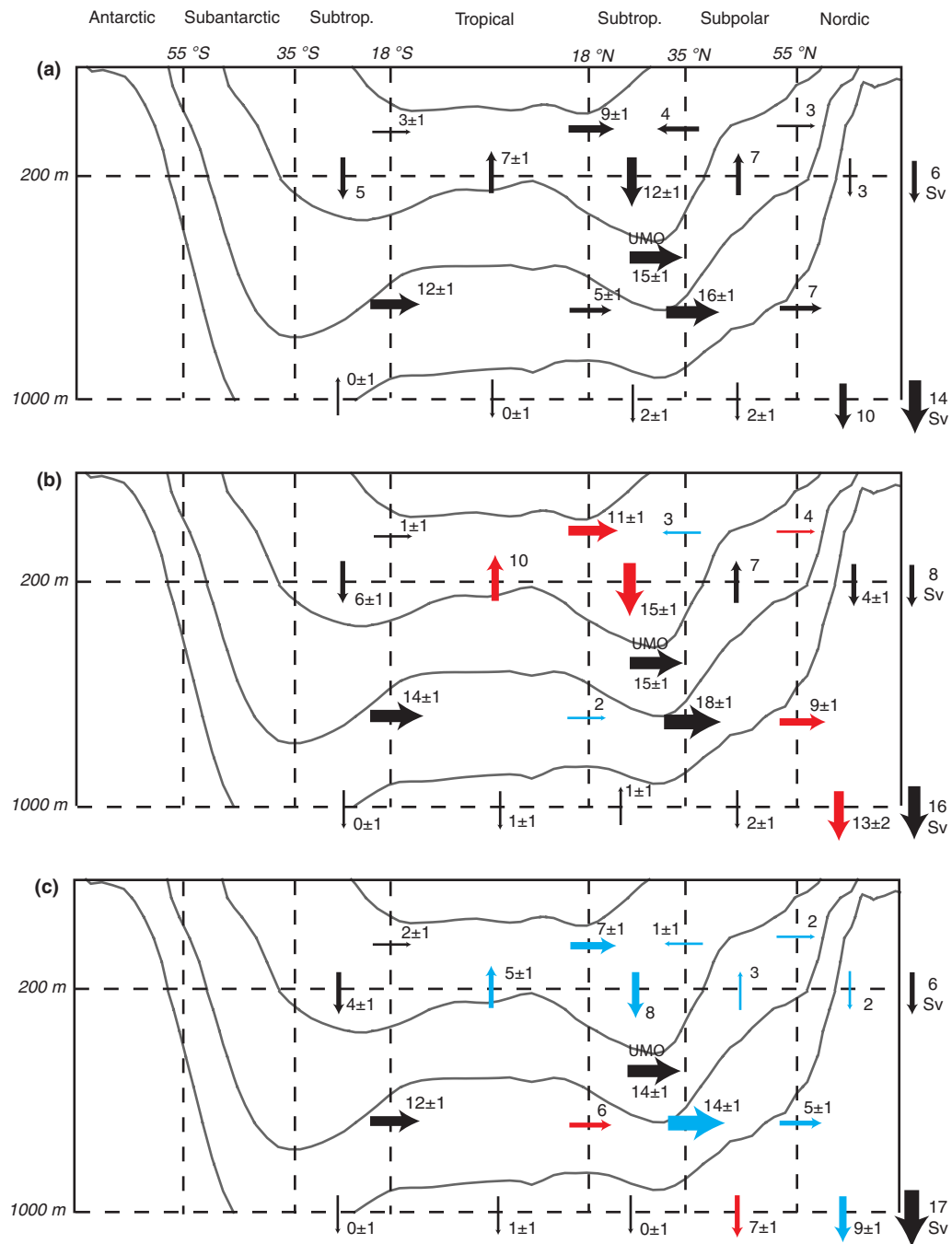
Data sources. Data for the assimilation model were obtained from the World Ocean Database 2013 (temperature and salinity), available at <https://www.nodc.noaa.gov/OC5/WOD13/>, and the GLODAPv2 database⁴⁰ (radiocarbon and CFCs) are archived at the Carbon Dioxide Information Analysis Center (CDIAC; <http://cdiac.ornl.gov/oceans/GLODAPv2/>). Mapped SST³⁶ and salinity³⁵ climatologies were obtained from the 2009 World Ocean Atlas at https://www.nodc.noaa.gov/OC5/WOA09/pr_woa09.html. The NOAA_ERSST_v4⁵² and COBE-SST⁵¹ data are provided by the NOAA/OAR/ESRL PSD, Boulder, Colorado, USA,

from their website at <http://www.esrl.noaa.gov/psd/>. NCEP reanalysis data were obtained from <http://www.esrl.noaa.gov/psd/data/gridded/data.ncep.reanalysis.surfaceflux.html>. The Mauna Loa CO₂ record used in our carbon cycle model is available at the NOAA Earth System Research Laboratory at <http://www.esrl.noaa.gov/gmd/ccgg/trends/>. Data from the SOCOM project^{4,5,15,53–63} are available at <http://www.bgc-jena.mpg.de/SOCOM/>.

Data availability. All data used to create the figures in this paper will be archived at CDIAC (<http://cdiac.ornl.gov/>).

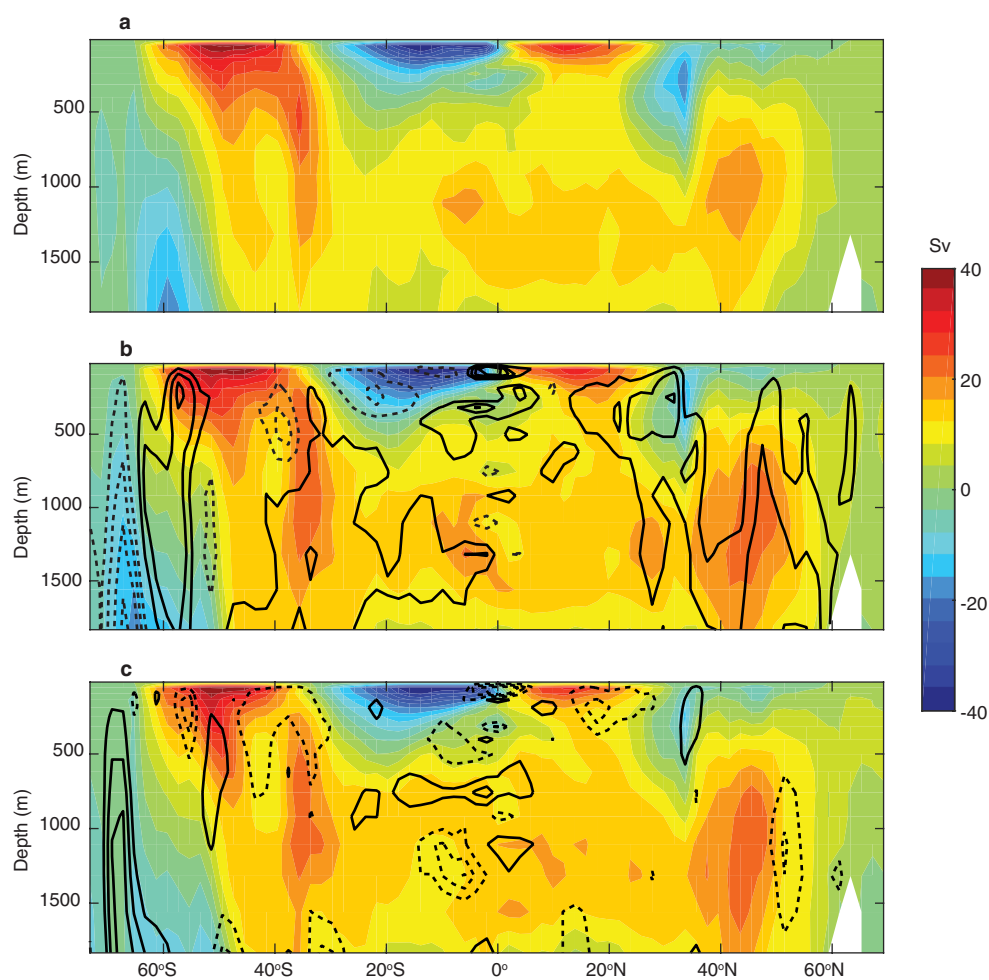
Code availability. Code may be obtained by contacting T.D. (tdevries@geog.ucsb.edu).

30. Olsen, A. *et al.* The Global Ocean Data Analysis Project version 2 (GLODAPv2)—an internally consistent data product for the world ocean. *Earth System Sci. Data* **8**, 297–323 (2016).
31. Wanninkhof, R. Relationship between wind speed and gas exchange over the ocean. *J. Geophys. Res.* **97**, 7373–7382 (1992).
32. Najjar, R. & Orr, J. Design of OCMIP-2 simulations of chlorofluorocarbons, the solubility pump and common biogeochemistry. <http://www.cgd.ucar.edu/oce/OCMIP/design.pdf> (1998).
33. Bullister, J. L. Atmospheric CFC-11, CFC-12, CFC-113, CCl₄, and SF₆ histories (1910–2014). NOAA technical report. http://cdiac.esd.ornl.gov/oceans/new_atmCFC.html (Carbon Dioxide Information Analysis Centre, NOAA, 2014).
34. Warner, M. & Weiss, R. Solubilities of chlorofluorocarbons 11 and 12 in water and seawater. *Deep-Sea Res. A* **32**, 1485–1497 (1985).
35. Antonov, J. I. *et al.* in *World Ocean Atlas 2009 Vol. 2 Salinity* (ed. Levitus, S.) 1–184 (US Government Printing Office, 2010).
36. Locarnini, R. A., Mishonov, A. V., Antonov, J. I., Boyer, T. P. & Garcia, H. E. in *World Ocean Atlas 2009 Vol. 1 Temperature* (ed. Levitus, S.) 1–184 (US Government Printing Office, 2010).
37. Fiadeiro, M. E. Three-dimensional modeling of tracers in the deep Pacific Ocean, II. Radiocarbon and the circulation. *J. Mar. Res.* **40**, 537–550 (1982).
38. Sweeney, C. *et al.* Constraining global air-sea gas exchange for CO₂ with recent bomb ¹⁴C measurements. *Glob. Biogeochem. Cycles* **21**, GB2015 (2007).
39. Najjar, R. G. *et al.* Impact of circulation on export production, dissolved organic matter, and dissolved oxygen in the ocean: results from Phase II of the Ocean Carbon-cycle Model Intercomparison Project (OCMIP-2). *Glob. Biogeochem. Cycles* **21**, GB3007 (2007).
40. Kwon, E. Y. & Primeau, F. Optimization and sensitivity of a global biogeochemistry ocean model using combined in situ DIC, alkalinity, and phosphate data. *J. Geophys. Res.* **113**, C08011 (2008).
41. Graven, H. D., Gruber, N., Key, R., Khattiwala, S. & Giraud, X. Changing controls on oceanic radiocarbon: New insights on shallow-to-deep ocean exchange and anthropogenic CO₂ uptake. *J. Geophys. Res.* **117**, C10005 (2012).
42. Martin, J., Knauer, G., Karl, D. & Broenkow, W. VERTEX: carbon cycling in the northeast Pacific. *Deep-Sea Res.* **34**, 267–285 (1987).
43. DeVries, T. & Deutsch, C. Large-scale variations in the stoichiometry of marine organic matter respiration. *Nat. Geosci.* **7**, 890–894 (2014).
44. DeVries, T., Deutsch, C., Rafter, P. & Primeau, F. Marine denitrification rates determined from a global 3-D inverse model. *Biogeosciences* **10**, 2481–2496 (2013).
45. Kwon, E. Y. & Primeau, F. Optimization and sensitivity study of a biogeochemistry ocean model using an implicit solver and in situ phosphate data. *Glob. Biogeochem. Cycles* **20**, GB4009 (2006).
46. Schlitzer, R. Carbon export fluxes in the southern ocean: results from inverse modeling and comparison with satellite-based estimates. *Deep-Sea Res. II* **49**, 1623–1644 (2002).
47. Primeau, F. On the variability of the exponent in the power law depth dependence of POC flux estimated from sediment traps. *Deep-Sea Res.* **53**, 1335–1343 (2006).
48. DeVries, T., Primeau, F. & Deutsch, C. The sequestration efficiency of the biological pump. *Geophys. Res. Lett.* **39**, L13601 (2012).
49. Jin, X., Gruber, N., Dunne, J., Sarmiento, J. & Armstrong, R. Diagnosing the contribution of phytoplankton functional groups to the production and export of particulate organic carbon, CaCO₃, and opal from global nutrient and alkalinity distributions. *Glob. Biogeochem. Cycles* **20**, GB2015 (2006).
50. Redfield, A. C. The biological control of chemical factors in the environment. *Am. Sci.* **46**, 205–221 (1958).
51. Hirahara, S., Ishii, M. & Fukuda, Y. Centennial-scale sea surface temperature analysis and its uncertainty. *J. Clim.* **27**, 57–75 (2014).
52. Huang, B. *et al.* Extended reconstructed sea surface temperature version 4 (ersst. v4). Part I: upgrades and intercomparisons. *J. Clim.* **28**, 911–930 (2015).
53. Jones, S. D., Le Quééré, C., Rödenbeck, C., Manning, A. C. & Olsen, A. A statistical gap-filling method to interpolate global monthly surface ocean carbon dioxide data. *J. Adv. Model. Earth Syst.* **7**, 1554–1575 (2015).
54. Shutler, J. D. *et al.* Fluxengine: a flexible processing system for calculating atmosphere–ocean carbon dioxide gas fluxes and climatologies. *J. Atmos. Ocean. Technol.* **33**, 741–756 (2016).
55. Rödenbeck, C. *et al.* Global surface-ocean p(CO₂) and sea-air CO₂ flux variability from an observation-driven ocean mixed-layer scheme. *Ocean Sci.* **9**, 193–216 (2013).
56. Park, G.-H. *et al.* Variability of global net sea–air CO₂ fluxes over the last three decades using empirical relationships. *Tellus B* **62**, 352–368 (2010).
57. Schuster, U. *et al.* An assessment of the Atlantic and Arctic sea-air CO₂ fluxes, 1990–2009. *Biogeosciences* **10**, 607–627 (2013).
58. Iida, Y. *et al.* Trends in pCO₂ and sea–air CO₂ flux over the global open oceans for the last two decades. *J. Oceanogr.* **71**, 637–661 (2015).
59. Sasse, T., McNeil, B. & Abramowitz, G. A novel method for diagnosing seasonal to inter-annual surface ocean carbon dynamics from bottle data using neural networks. *Biogeosciences* **10**, 4319–4340 (2013).
60. Peylin, P. Carbones: 30-year reanalysis of carbon fluxes and pools over Europe and the globe. <http://www.carbones.eu/wcmqs/> (accessed 11 January 2017).
61. Nakaoka, S. *et al.* Estimating temporal and spatial variation of ocean surface pCO₂ in the North Pacific using a self-organizing map neural network technique. *Biogeosciences* **10**, 6093–6106 (2013).
62. Zeng, J., Nojiri, Y., Landschützer, P., Telszewski, M. & Nakaoka, S. A global surface ocean fCO₂ climatology based on a feed-forward neural network. *J. Atmos. Ocean. Technol.* **31**, 1838–1849 (2014).
63. Valsala, V. & Maksyutov, S. Simulation and assimilation of global ocean pCO₂ and air–sea CO₂ fluxes using ship observations of surface ocean pCO₂ in a simplified biogeochemical offline model. *Tellus B* **62**, 821–840 (2010).



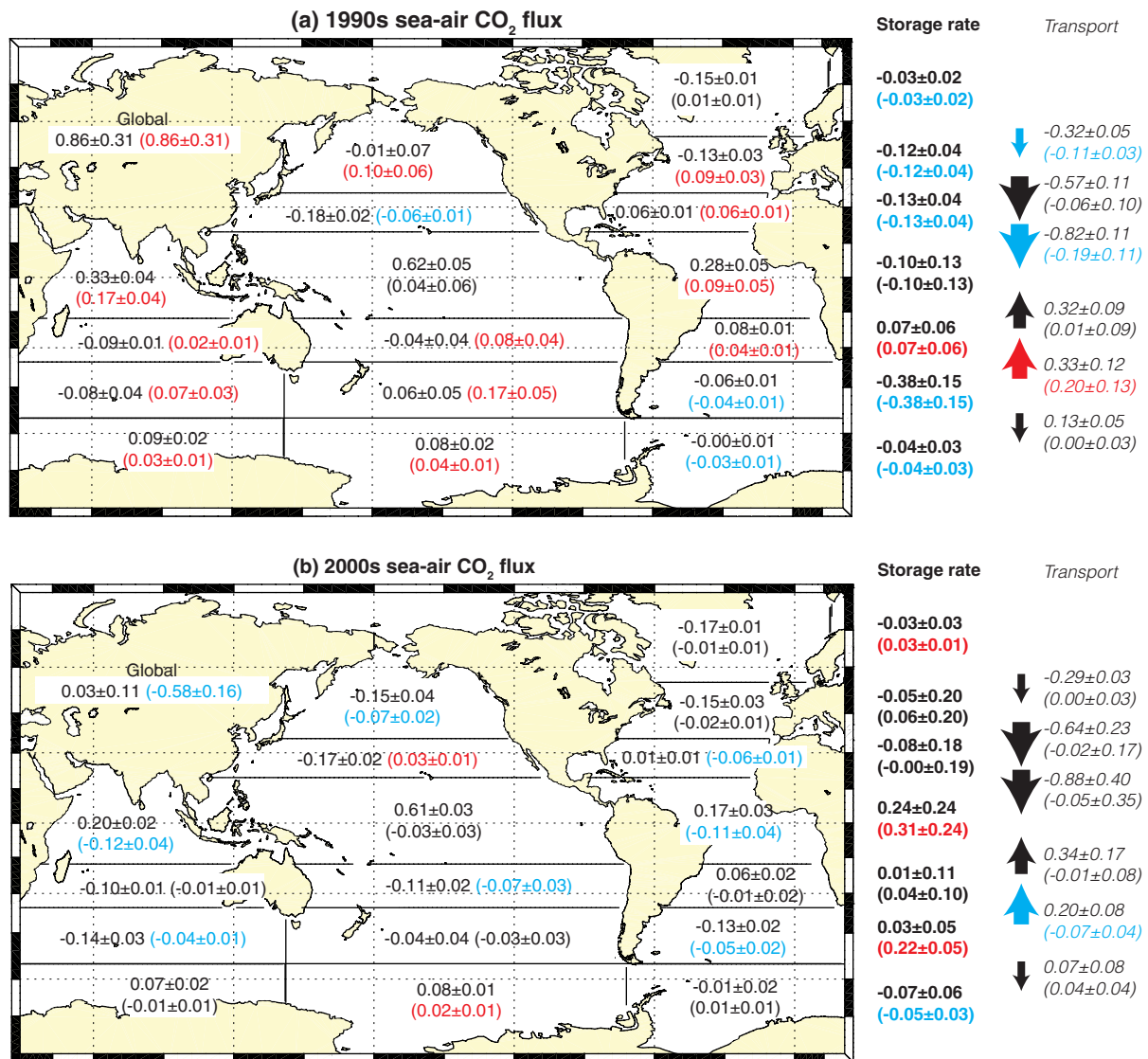
Extended Data Figure 1 | Atlantic Ocean upper-ocean overturning circulation. Same as Fig. 1 (transports in Sv), but for circulation in the Atlantic Ocean north of 35° S. Net transports across 200 m and 1,000 m are shown to the right of each diagram for each period. Also shown is the

upper-mid ocean (UMO) transport (northward ocean transport integrated from the surface to 1,000 m) at 26° N, for comparison with previous studies of Atlantic Meridional Overturning Circulation variability²¹. Uncertainties as in Fig. 1.

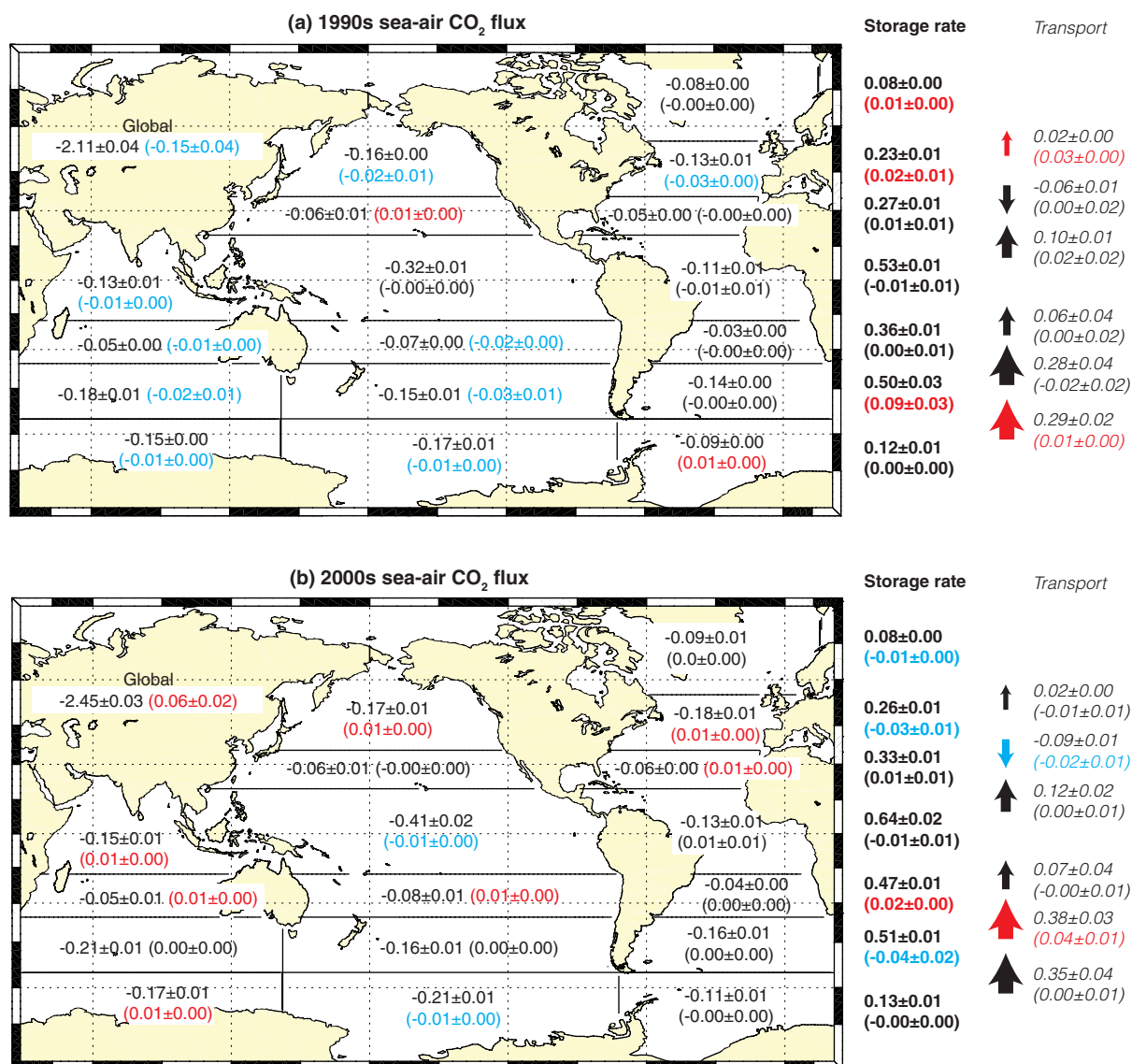


Extended Data Figure 2 | Global meridional overturning circulation variability over three decades. Colours show the global ocean meridional overturning circulation (MOC) above 1,800 m for the 1980s (a), the 1990s (b), and the 2000s (c). Positive numbers represent clockwise circulation, and negative numbers counterclockwise circulation. The contour interval

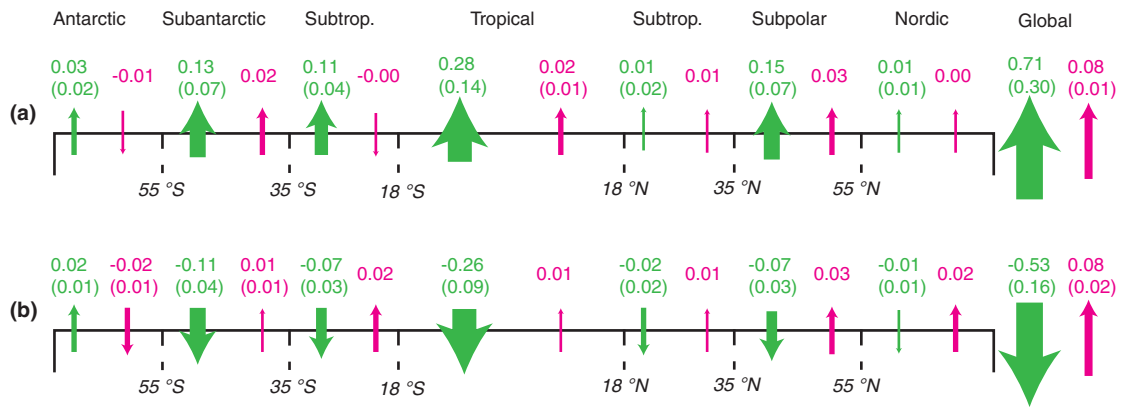
is 4 Sv. The black contours superimposed on b and c show the difference between the MOC in each decade and the prior decade. Negative differences are shown as dashed contours, positive differences as solid contours, with a contour interval of 3 Sv. Contours are drawn only where the absolute difference is greater than or equal to 3 Sv.



Extended Data Figure 3 | Air-sea fluxes, transports, and storage rates of natural CO₂. Same as Fig. 2, but for natural CO₂ only. Units are Pg C yr⁻¹.

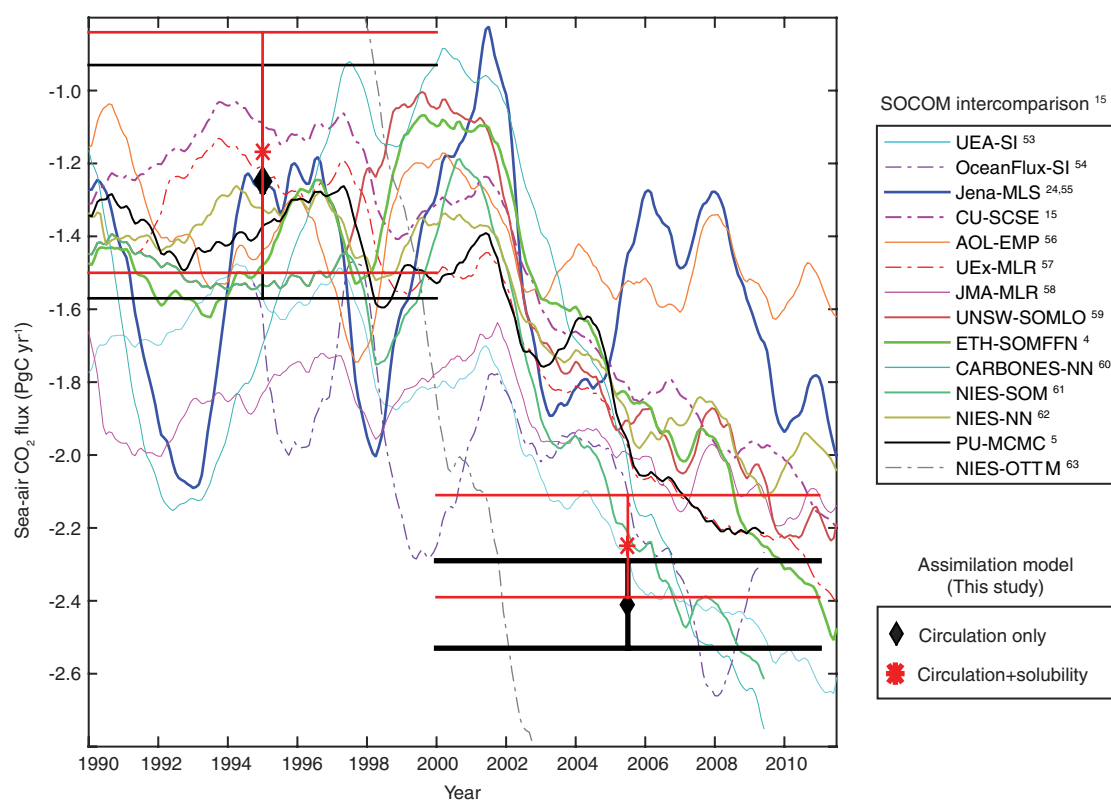


Extended Data Figure 4 | Air-sea fluxes, transports, and storage rates of anthropogenic CO₂. Same as Fig. 2, but for anthropogenic CO₂ only. Units are Pg C yr⁻¹.



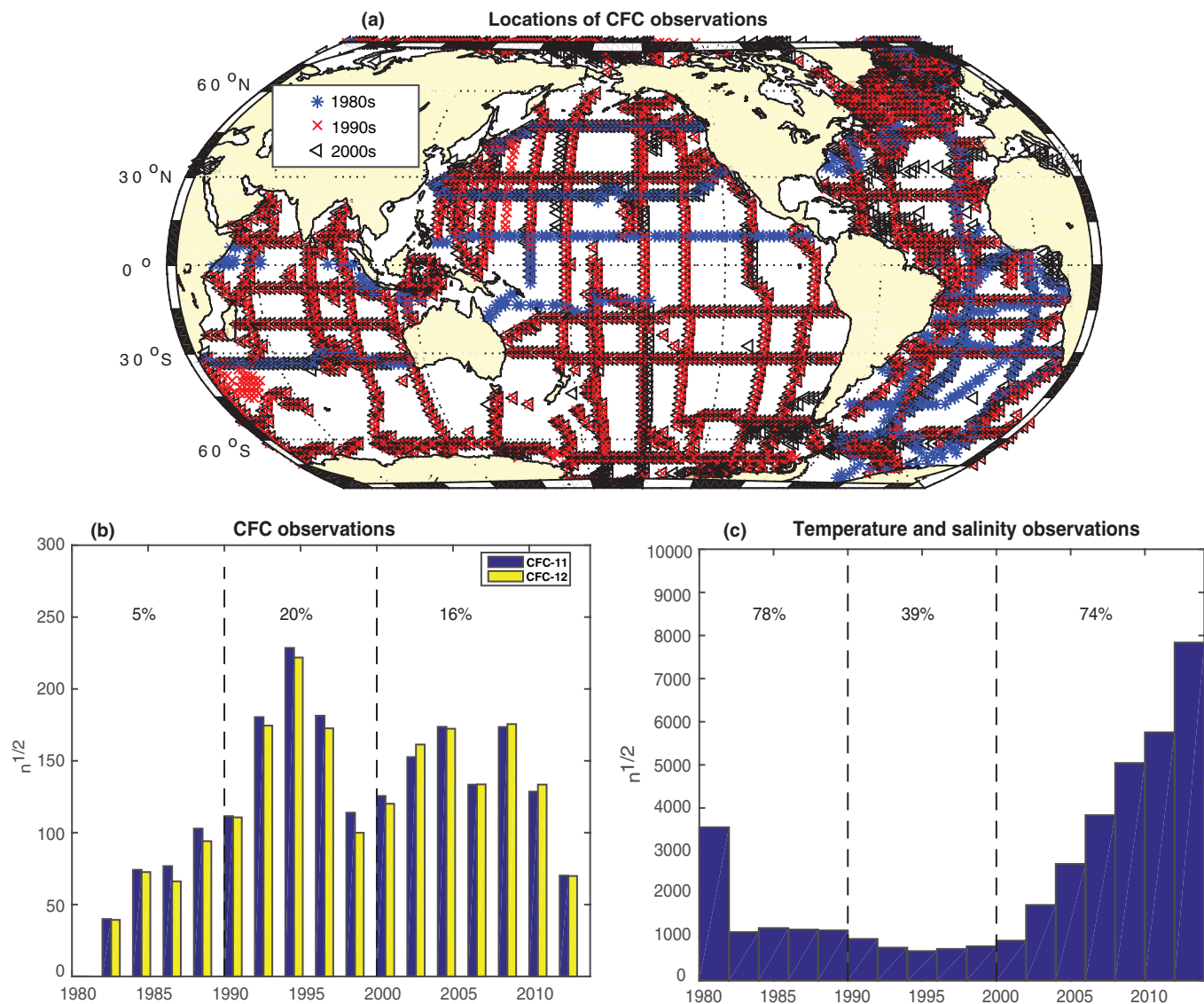
Extended Data Figure 5 | Comparison of circulation-induced and solubility-induced changes in CO₂ flux. For the decades of the 1990s (a) and 2000s (b), green arrows and lettering show the zonally integrated anomalous air–sea CO₂ flux (Pg C yr⁻¹, negative values indicate ocean uptake) due to circulation variability, calculated by comparing the air–sea CO₂ flux within each decade to what it would have been had circulation remained unchanged from the previous decade. Uncertainties were

calculated as in Fig. 2. Magenta arrows and lettering show the zonally integrated anomalous air–sea CO₂ flux due to temperature-driven changes in solubility, calculated by comparing simulations with constant SST and decadal varying SST. Uncertainties (one standard deviation) were calculated by propagating two different SST reconstructions in our suite of five different circulation models (see Methods).



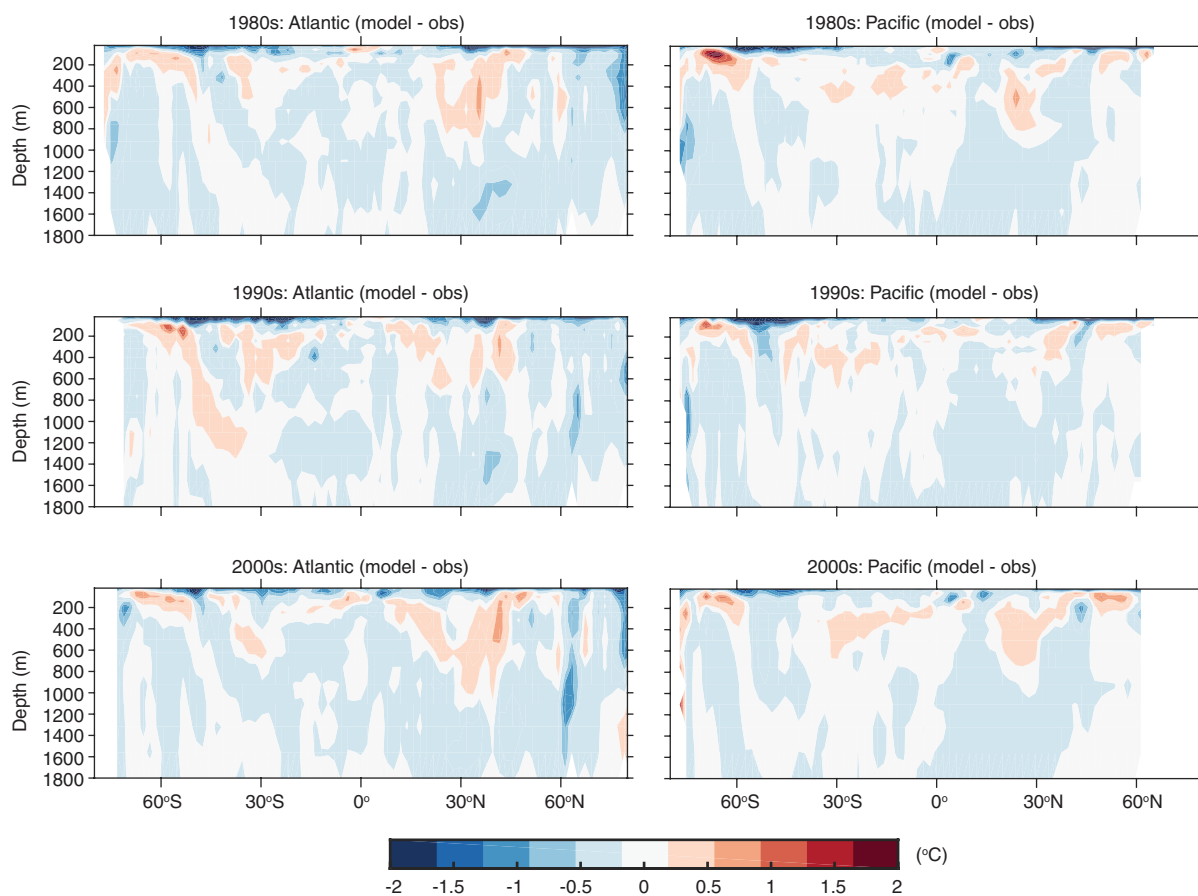
Extended Data Figure 6 | Comparison of SOCOM and assimilation model oceanic CO₂ uptake. Curves show the interannually-varying global sea-air CO₂ flux (negative into ocean) from the models participating in the SOCOM intercomparison¹⁵. Symbols with error bars are the decadal averaged sea-air CO₂ fluxes estimated from our data-assimilated ocean circulation model. One version of our assimilation model includes the

effects of circulation as captured by the decadal averaged circulation model (black diamonds, as presented in main text), while the other additionally includes solubility effects due to decadal SST changes (red star, Extended Data Fig. 5). Uncertainties calculated as in Fig. 2 and Extended Data Fig. 5. Data are from refs 4, 5, 15, 24 and 53–63.

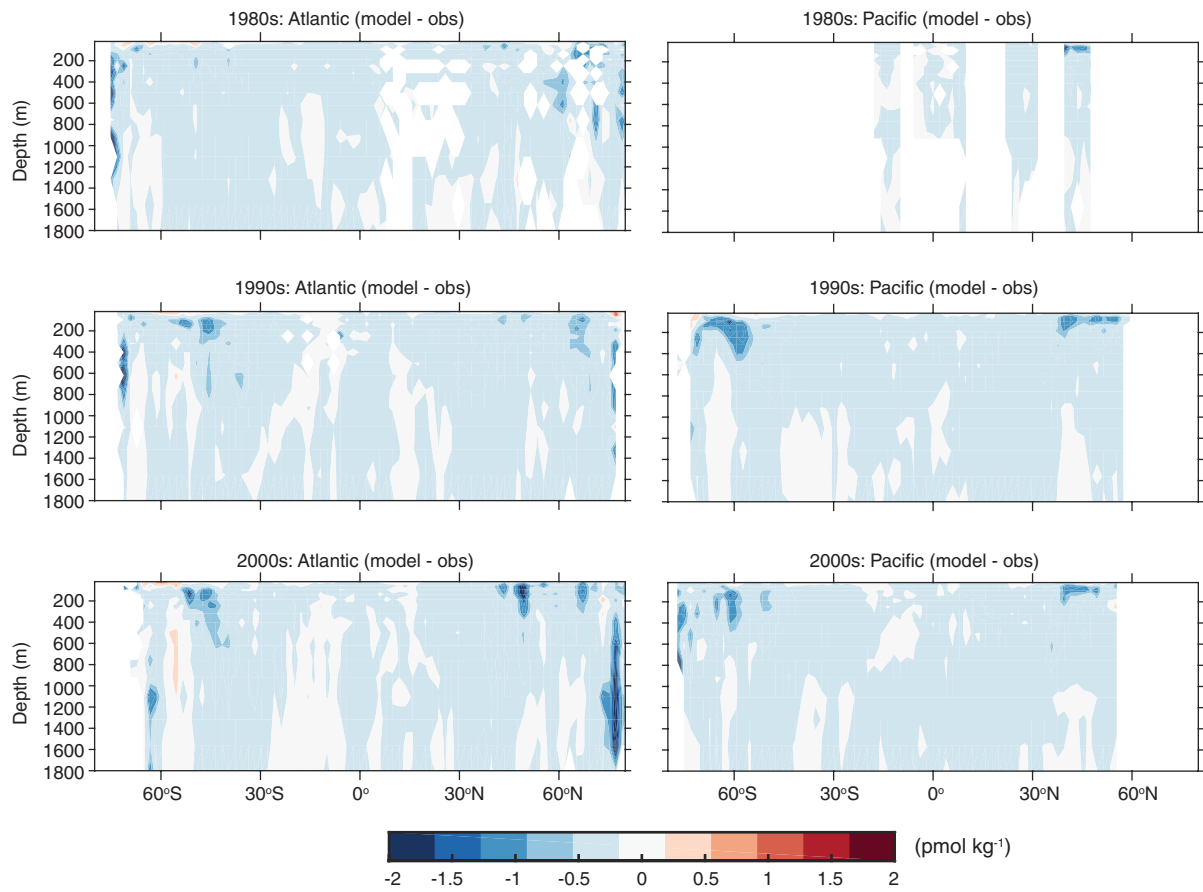


Extended Data Figure 7 | The distribution of observations used to constrain the data assimilation model. **a**, Spatial distribution of CFC (CFC-11 and CFC-12) observations during each assimilation time period. **b**, Distribution of CFC-11 (blue) and CFC-12 (yellow) observations over time, binned at 2-year intervals (where n is the number of observations

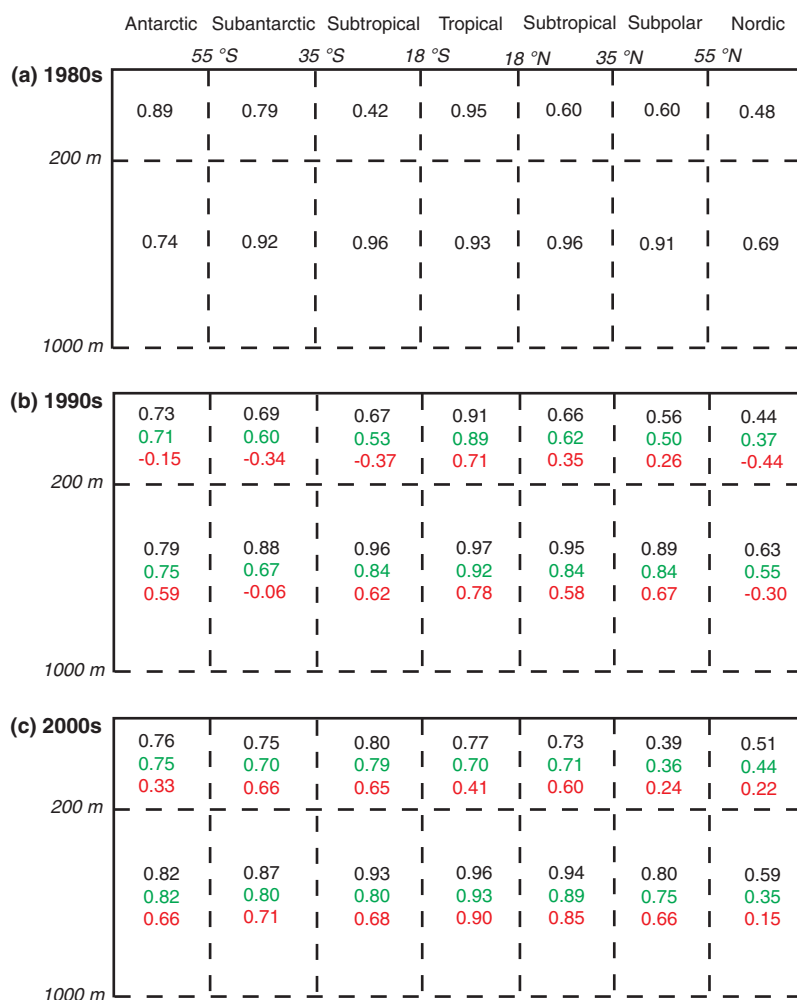
within each interval). The printed percentages in each assimilation time period indicate the percentage of model grid points that have a CFC-11 or CFC-12 observation during that period. **c**, Distribution of paired temperature and salinity observations over time, in 2-year bins. Observations before 1980 are included in the 1980–1982 bin.



Extended Data Figure 8 | Model-data residuals for potential temperature. Zonally averaged model-data residuals for the Atlantic (left) and Pacific (right) basins for the three assimilation time periods. Contour interval is 0.25 °C. Positive values indicate that modelled potential temperature is higher than observed (obs).



Extended Data Figure 9 | Model-data residuals for CFC-11. Zonally averaged model-data residuals for the Atlantic (left) and Pacific (right) basins for the three assimilation time periods. Contour interval is 0.25 pmol kg⁻¹. Positive values indicate that modelled CFC-11 is higher than observed.



Extended Data Figure 10 | Comparison of circulations tailored separately for each decadal period to piecewise constant and to unchanging circulations. The quality of a circulation is quantified by using it to propagate CFC-11 and computing the R^2 between modelled and observed CFC-11 concentrations for each region and time period. Colours indicate different circulations. The black R^2 values for a given time period were calculated using the circulation that was data-assimilated

for that period and held steady throughout the CFC propagation. Green R^2 values are obtained if we change the circulation on the fly from decade to decade, as we did for the CO_2 simulations. Red R^2 values are obtained if the circulation in the 1990s (2000s) was held constant at the 1980s (1990s) levels. The green R^2 values are much higher than the red R^2 values, verifying that a decadal varying circulation fits the observed CFC concentrations much better than an unchanging circulation.